Geophysical Research Letters

RESEARCH LETTER
10.1029/2023GL106170

Seismic Evidence for Craton Formation by Underplating and Development of the MLD

Alistair Boyce[1], Thomas Bodin[1], Stéphanie Durand[1], Dorian Soergel[1,2], and Eric Debayle[1]

[1]Université Claude Bernard Lyon 1, ENS de Lyon, CNRS, UMR 5276 LGL-TPE, Villeurbanne, France, [2]Department of Earth and Planetary Science, University of California, Berkeley, Berkeley, CA, USA

Key Points:

- Bayesian surface wave inversion reconciles existing differences between seismic images of craton structure from long and short period data
- Cratons show a shallow low velocity zone (LVZ) within a layer of positive radial anisotropy and a high velocity isotropic layer beneath
- Cratons are formed in two stages shown by anisotropic structure and are later modified producing a LVZ and mid lithosphere discontinuities

Supporting Information:

Supporting Information may be found in the online version of this article.

Correspondence to:

A. Boyce,
alistair.boyce@univ-lyon1.fr

Citation:

Boyce, A., Bodin, T., Durand, S., Soergel, D., & Debayle, E. (2024). Seismic evidence for craton formation by underplating and development of the MLD. *Geophysical Research Letters*, *51*, e2023GL106170. https://doi.org/10.1029/2023GL106170

Received 30 AUG 2023
Accepted 10 JAN 2024

Author Contributions:

Conceptualization: Alistair Boyce, Thomas Bodin, Stéphanie Durand
Data curation: Stéphanie Durand, Eric Debayle
Formal analysis: Alistair Boyce
Funding acquisition: Thomas Bodin, Eric Debayle
Investigation: Alistair Boyce
Methodology: Alistair Boyce, Thomas Bodin, Stéphanie Durand, Dorian Soergel
Project Administration: Thomas Bodin
Resources: Thomas Bodin
Software: Alistair Boyce, Thomas Bodin, Stéphanie Durand, Dorian Soergel

Abstract Inconsistencies between observations from long and short period seismic waves and geochemical data mean craton formation and evolution remains enigmatic. Specifically, internal layering and radial anisotropy are poorly constrained. Here, we show that these inconsistencies can be reconciled by inverting cratonic Rayleigh and Love surface wave dispersion curves for shear-wave velocity and radial anisotropy using a flexible Bayesian scheme. This approach requires no explicit vertical smoothing and only adds anisotropy to layers where required by the data. We show that all cratonic lithospheres are comprised of a positively radially anisotropic upper layer, best explained by Archean underplating, and an isotropic layer beneath, indicative of two-stage formation. Within the positively radially anisotropic upper layer, we find a variable amplitude low velocity zone within 9 of 12 cratons studied, that is well correlated with observed Mid-Lithospheric Discontinuities (MLDs). The MLD is best explained by metasomatism after craton formation.

Plain Language Summary The ancient cores of the continents, or cratons, are a treasure-trove of >2.5 billion years of Earth's history. However, scientists disagree on the processes that led to their formation, or whether they have evolved significantly through time. This is because the geological and geophysical methods used to investigate cratons often yield conflicting results. By capitalizing on an up-to-date global long-wavelength seismic data set, we image the cores of 12 cratons using an advanced statistical method, Bayesian inference. The flexible method requires few choices to be made a priori, is driven by the quality of the data itself and measures uncertainties on results. By detecting velocity differences between horizontally and vertically vibrating seismic waves, we show that all cratons likely comprise an upper layer formed during the hot early Earth, by a process that strongly aligns the constituent minerals of the rocks in the horizontal plane. Below this ∼125 km thick upper layer, a lower layer (∼150 km thick) shows no clear alignment of minerals and so was likely formed by a different process, at a later time. Variable slow wavespeed zones exist within the upper layer that match previous results from short-wavelength seismic data.

1. Introduction

The formation and subsequent evolution of cratons, the cold, thick, ancient cores of the continents, remain controversial because a unifying theory is lacking (e.g., Aulbach, 2012; Griffin et al., 2003; Hoffman, 1990; Jordan, 1978; Lee et al., 2011; Priestley et al., 2020). The debate centers on the apparent spatial variability in seismically imaged and geochemically sampled cratonic cores, and incompatibilities between different data types and tomographic inversion schemes. For example, active and ancient geological processes such as flow/deformation can be constrained by mapping radial anisotropy, the velocity ratio between horizontally traveling shear waves that are polarized horizontally and vertically (where positive anisotropy indicates horizontally aligned fabrics and negative anisotropy indicates vertically aligned fabrics; Auer et al., 2014; Chang et al., 2015; Kustowski et al., 2008; Lekić & Romanowicz, 2011; Megnin & Romanowicz, 2000; Panning et al., 2010). However, these global images are especially inconsistent (e.g., Chang et al., 2014; Figure 1, Figures S1–S5 in Supporting Information S1), meaning we cannot reliably interpret them for craton evolution. Some models indicate negative radial anisotropy only occurs within continental lithosphere at ∼150 km depth (e.g., Priestley et al., 2020). This suggests vertically oriented fabrics, interpreted as evidence for craton formation by horizontal terrane accretion and arc thickening. Meanwhile, other models (e.g., Lekić & Romanowicz, 2011) reveal pervasive positive radial anisotropy in this depth range, implying horizontally oriented fabrics, perhaps more consistent with craton formation by underplating (Arndt et al., 2009; Griffin et al., 2003).

Supervision: Thomas Bodin, Stéphanie Durand, Eric Debayle
Validation: Alistair Boyce
Visualization: Alistair Boyce
Writing – original draft: Alistair Boyce
Writing – review & editing: Alistair Boyce, Thomas Bodin, Stéphanie Durand, Dorian Soergel, Eric Debayle

Moreover, while global shear-wave velocity models based on long period data show that cratons are consistently characterized by smooth high velocity anomalies that extend to ∼250 km depth (e.g., Auer et al., 2014; Chang et al., 2015; Debayle & Kennett, 2000; Debayle & Ricard, 2012; Kustowski et al., 2008; Lekić & Romanowicz, 2011; Megnin & Romanowicz, 2000; Panning et al., 2010; Figure 1, Figures S4 and S5 in Supporting Information S1), these results are difficult to interpret alongside geochemical evidence that suggests cratons possess significant internal layering (e.g., Aulbach et al., 2017; Griffin et al., 1999). Furthermore, short period converted seismic phases (e.g., S-to-p) frequently highlight a negative velocity gradient (NVG) at ∼70–130 km depth within cratons, often referred to as the mid-lithospheric discontinuity (MLD; e.g., Abt et al., 2010; L. Chen, 2017; Ford et al., 2010; Fu et al., 2022; Hopper & Fischer, 2015; Karato et al., 2015; Krueger et al., 2021; Levin et al., 2023; Miller & Eaton, 2010; Rader et al., 2015; Selway et al., 2015; Sodoudi et al., 2013; Wittlinger & Farra, 2007; Wölbern et al., 2012). However, a corresponding low velocity zone (LVZ) in global scale tomographic models is rarely observed (Figure 1; Figures S4 and S5 in Supporting Information S1), meaning we cannot determine the ubiquity of this feature, and therefore, its role in craton development.

Here, we reconcile these observations by inverting surface wave measurements with a flexible Bayesian approach. Specifically, we extract Rayleigh and Love fundamental and first-to-fifth overtone surface wave dispersion curves for 12 individual cratons from an up-to-date database of global phase velocity maps (Durand et al., 2015; Ho et al., 2016). We jointly invert these data, at each specific point in 1D for shear velocity and radial anisotropy using a Bayesian scheme (Bodin et al., 2012, 2016). This has two key benefits. First, the Bayesian inversion requires no explicit vertical smoothing or linearization around a reference velocity model. Second, our transdimensional parameterization, where the number of model parameters is unknown, only adds anisotropy to layers where required by the data (Alder et al., 2021; H. Yuan & Bodin, 2018). Results show that LVZs may exist within the majority of cratons (9 of 12 studied), which are very well correlated in depth to NVGs observed by converted phases studies (e.g., Rader et al., 2015). Furthermore, cratonic radially anisotropic structure is remarkably consistent. All continental cores are comprised of a positively radially anisotropic upper layer, with an isotropic layer beneath. Our robust images of seismic cratonic structure facilitate improved insights into craton formation and evolution processes.

2. Data and Methods

2.1. Surface Wave Dispersion Curves

Our data set comprises global Rayleigh and Love surface wave phase velocity maps, from the fundamental mode up to fifth overtone, for periods ranging from 40 to 200 s, sourced from Durand et al. (2015) and Ho et al. (2016). From these phase velocity maps, we extract dispersion curves from 12 selected point locations within cratons (Figure S6 in Supporting Information S1). To facilitate global comparison, we extract dispersion curves from five tectonically active regions and a cross section through continental North America (Figures S7 and S8 in Supporting Information S1). Because the phase velocity maps are themselves the result of a 2D regularized inversion, with a correlation length of 400 km (Durand et al., 2015), we only extract dispersion curve data from points within well resolved features with >900 km separation.

2.2. Bayesian Inversion

We jointly invert Rayleigh and Love dispersion curves for 1D posterior distributions of V_{SV}, radial anisotropy ($\xi = V_{SH}^2/V_{SV}^2$, where V_{SV} and V_{SH} are vertical and horizontally polarized S-wave velocity) and V_{PH} (horizontally traveling P-velocity) using a Bayesian transdimensional Markov chain Monte Carlo hierarchical scheme, following (Bodin et al., 2016). Including V_{PH} in our inversions improves synthetic model recovery and reduces bias in V_{SV} and ξ results (see Text S6 in Supporting Information S1 for discussion). We invert the data between 700 km depth and the surface, including the crust, to avoid possible anisotropic artifacts (e.g., Bozdağ & Trampert, 2008). However, given the 40 s minimum period of our data set and corresponding sensitivity peak at ∼50 km (Figure S9 in Supporting Information S1), we limit interpretation to structure below the crust. We thus seek robust recovery of mantle seismic parameters using this 1D method because a global inversion would be prohibitively expensive.

Within a Bayesian framework, we use a uniform prior probability distribution where the mean value at each depth follows an isotropic PREM-like model (Dziewonski & Anderson, 1981) smoothed into a local crustal model sourced from CRUST1.0 (Laske et al., 2013, see Text S3 in Supporting Information S1). Prior distributions

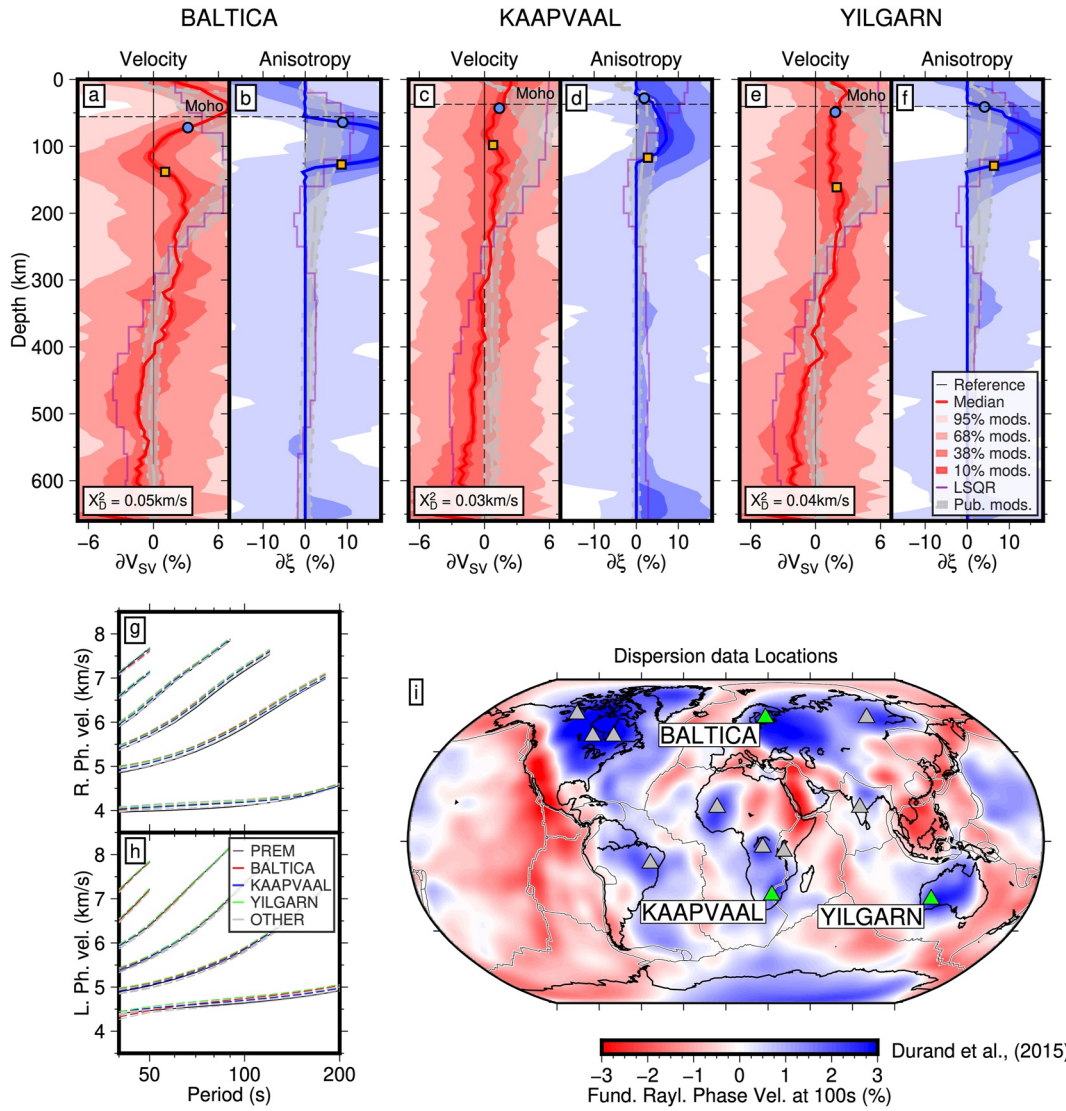

Figure 1. Posterior distributions from Bayesian inversion for V_{SV} and ξ for Baltica (a, b), Kaapvaal (c, d) and Yilgarn (e, f) with respect to an isotropic reference model smoothed into Crust1.0 (black line). The preferred median model for V_{SV} (red) and ξ (blue) is shown as a solid, bold line. Confidence intervals (percentage of models) are shown as varying shades of red (V_{SV}) and blue (ξ). Data misfit $\left(X_D^2\right)$ is also reported. Transition depths (blue circles, orange squares) used in Figure 2 also shown. Gray shaded region marks one standard deviation (dotted) from the mean (dashed) of V_{SV} and ξ profiles extracted from 12 radially anisotropic tomographic models in each location (Figures S1–S5 in Supporting Information S1). Tomographic models: *Durand—unpublished*, CAM2016 (Priestley et al., 2020), SEMum (Lekić & Romanowicz, 2011), SAVANI (Auer et al., 2014), S362WMANI (Kustowski et al., 2008), S362ANI (Kustowski et al., 2008), S362ANI_M (Moulik & Ekström, 2014), SAW642AN (Megnin & Romanowicz, 2000), SAW642ANb (Panning et al., 2010), SEMUCB_WM1 (French & Romanowicz, 2014), SGLOBErani (Chang et al., 2015), SPani (Tesoniero et al., 2015). LSQR joint inversions for V_{SV} and ξ (V_{PH} fixed) are also shown (purple line). Rayleigh (g) and Love (h) fundamental and overtone (1–5) dispersion curves used in the inversions. (i) Fundamental mode Rayleigh wave phase velocity map at 100 s period from Durand et al. (2015), with three cratonic locations shown (green triangles). Results for nine other cratons (gray triangles) in Supporting Information S1 (Figures S16 and S17).

have a range of ±20%, ±40%, and ±40% around this model for V_{SV}, ξ, and V_{PH}, respectively. Inversions are run on 280 independent chains, whose starting model is randomly selected from a uniform distribution limited to half the width of the full prior. The first 300,000 iterations are discarded and we retain one sample in every 50 from the remaining 300,000 iterations to approximate the posterior probability distribution. The forward calculation of dispersion curves is executed by normal mode summation for each proposed velocity model using Mineos (Masters et al., 2011), rather than through the use of kernels (e.g., Beghein & Trampert, 2004). The

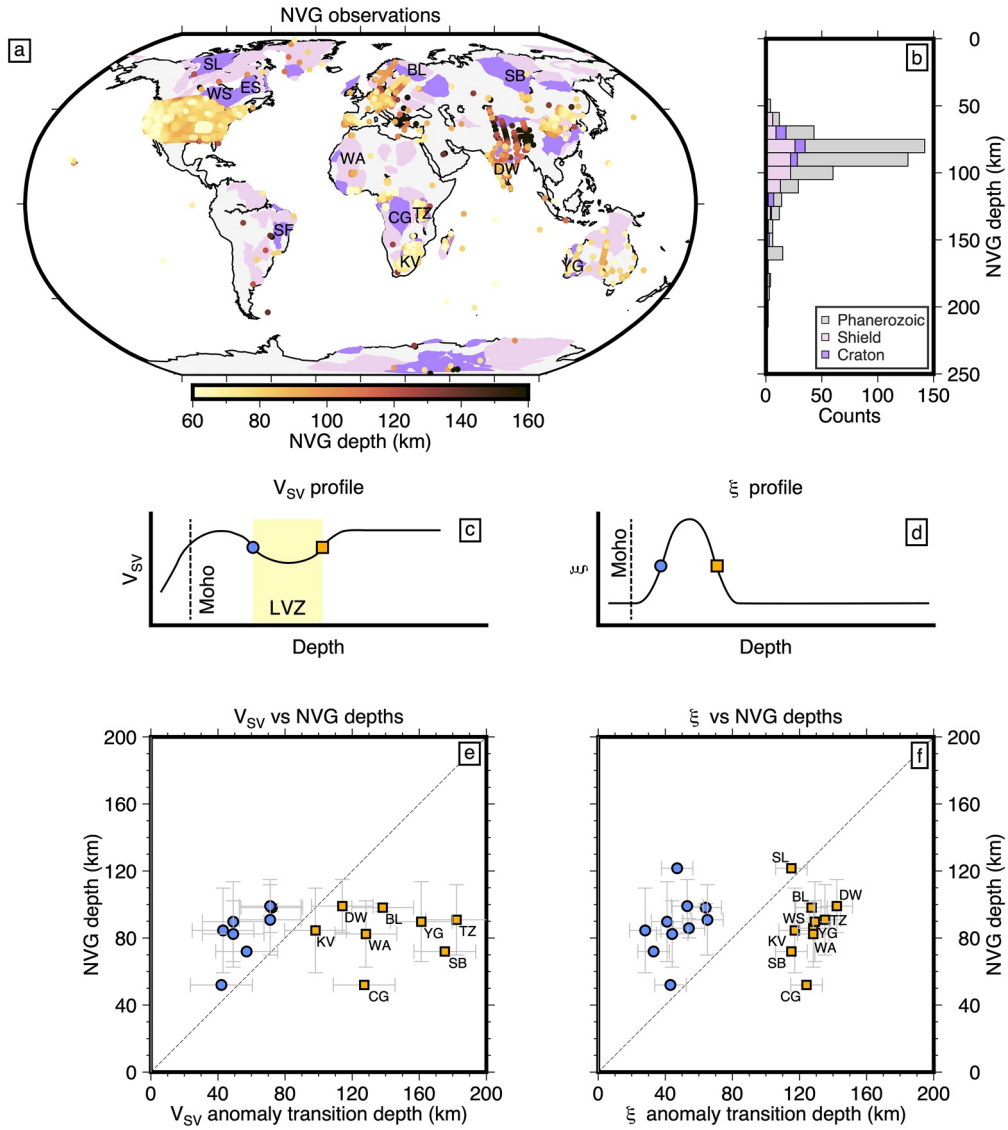

Figure 2. Global map negative velocity gradient (NVG) depth map obtained from short period S-to-P receiver functions. (a). Craton locations (purple) from Hasterok et al. (2022); BL: Baltica, CG: Congo, DW: Dharwar, ES: East Superior, KV: Kaapvaal, SF: Sao Francisco, SB: Siberia, SL: Slave, TZ: Tanzania, WA: West Africa, WS: West Superior, YG: Yilgarn. NVG depth histogram grouped by surface tectonics (b), Phanerozoic, Shield and Craton. NVG depths are averaged into 2° bins to avoid spatial sampling biases. For each craton with sufficient data, we extract transition depths (upper: blue circles, lower: orange squares) derived from maximum/minimum gradients below the Moho in the V_{SV} low velocity zone (LVZ) and positive $\delta\xi$ anomaly as shown in (c, d) and compare these to observed mean NVG depths (e, f). Vertical bars: one standard deviation uncertainty of NVG depths. Horizontal bars: estimated transition depth uncertainties.

transdimensional inversion allows addition or removal of layers within the model (between a range of 5 and 80), that can be isotropic or variably anisotropic (Alder et al., 2021; H. Yuan & Bodin, 2018). The hierarchical formulation means the level of data noise (i.e., the required level of data fit) for both Love and Rayleigh observations is treated as unknown (Bodin et al., 2012). We take the median value of the posterior solution at each depth as our preferred model and plot results with respect to the isotropic PREM-like model for visualization.

2.3. Least Squares Inversion

To compare our Bayesian results with standard inversion approaches, we also invert all dispersion data using the Tarantola and Valette (1982) LSQR scheme. We use the same isotropic PREM-like reference model for LSQR

inversions, as used for Bayesian inversions. However, we do not add CRUST1.0 (Laske et al., 2013) specific to each location at shallow depths. Instead, we simply vary crustal thickness within the reference model at each location. This choice dramatically decreases the impact of crustal thickness inaccuracies in the reference model when inverting for radial anisotropy (e.g., Chang et al., 2014). Sensitivity kernels appropriate for each reference model are calculated using Mineos (Masters et al., 2011).

We test variable parameterizations where data are inverted for V_{SV} and ξ independently (V_{PH} fixed), V_{SV} and ξ jointly (V_{PH} fixed), and V_{SV}, ξ and V_{PH} jointly. Optimal regularization parameters for the data and model covariance matrices, as well as the model correlation length (effective smoothing), are chosen by trade-off analysis, that aims to balance model smoothness against data fit.

2.4. Synthetic Tests

Initial synthetic tests (Figures S10–S15 in Supporting Information S1) examine the recovery of simple craton models in both Bayesian and LSQR inversion schemes and robustness of our parameterization. For each input model, dispersion curves of 0.0025 s Gaussian noise are forward modeled using Mineos (Masters et al., 2011), with identical data distribution to observed dispersion curves. Data are assigned random Gaussian observational errors of standard deviation 0.04 s. The Bayesian scheme recovers the input V_{SV} and ξ anomalies well. It is able to accurately recover a total absence of radial anisotropy and the vertical extent of lithospheric V_{SV} and ξ anomalies, with mean depth uncertainties of 18 and 9 km, respectively (Figures S10 and S11 in Supporting Information S1). Conversely, while LSQR inversions can reliably recover V_{SV} anomalies at upper mantle depths, ξ artifacts are produced in some cases where the input model is isotropic (i.e., $\xi = 1$, Figure S12 in Supporting Information S1). Our Bayesian approach is unaffected by crustal heterogeneity (Figure S13 in Supporting Information S1) and is a clear improvement over parameterizations that do not explicitly allow isotropic layers (Figure S14 in Supporting Information S1) or fix V_{PH} to a reference model (Figure S15 in Supporting Information S1). While V_{PH} often appears weakly constrained, broad confidence intervals typically render the true model within half the standard deviation from the mean model (e.g., Figure S10 in Supporting Information S1). These tests help explain the observed discrepancy between global radial anisotropy models (Figures S1–S5 in Supporting Information S1), and so motivate the use of our Bayesian scheme to study cratonic structure, despite the increased expense over LSQR inversions.

We seek a synthetic craton model that explains our results presented in Section 3 and observations from short period data (e.g., Rader et al., 2015). Consequently, we construct complex models that resemble results presented in Section 3, forward model data as above, and invert these data using the Bayesian scheme. We also compute synthetic seismograms through these models with accurate spectral element simulations using AxiSEM (Nissen-Meyer et al., 2014) with a minimum period of 5 s. We compute S-to-p receiver functions (SRFs) using iterative deconvolution (Ligorrìa & Ammon, 1999) with a Gaussian pulse width of 1.67 s (0.6 Hz) after filtering the data from 0.01 to 0.3 Hz. The source window spans 15 s before, to 15 s after the direct S phase, while the response window spans 55 s before, to 25 s after the direct phase. Finally, SRFs are stacked between 79 and 84° epicentral distance in the depth domain. Results of this analysis are presented in Section 4.

3. Results

3.1. Comparison of Bayesian and LSQR Inversion Results

Figure 1 shows three sets of V_{SV} and ξ posterior distributions from inversion of dispersion curves from the Baltica, Kaapvaal and Yilgarn cratons. Results from remaining cratons are given in Supporting Information S1 (Figures S16 and S17). Broadly, cratonic V_{SV} profiles are characterized by fast velocities above ~300 km depth and lower velocities below, consistent with the thickness of the seismic lithosphere imaged previously (e.g., Gung et al., 2003; Priestley et al., 2019). In detail however, the lithospheric velocity profiles are substantially rougher than previous results, with possible evidence for a low velocity zone (LVZ) at mid-lithospheric depths in the upper 150 km in 9 of 12 cratons (Figure 1; Figures S16 and S17 in Supporting Information S1). LVZs display variable amplitude (<3%), peak velocity reduction depth (37.01–115.2 km) and thickness (50 – 150+ km). An LVZ is clearly evident in Baltica, Congo, Kaapvaal, but is more subtle in Sao Francisco and Yilgarn cratons. Slave, Siberia, West Africa and West Superior show peak mantle velocities below 100 km depth, with lower velocities at shallower depths. East Superior displays a relatively constant lithospheric high velocity (2%–3%) to 300 km depth. Tanzania and Dharwar display slow velocities to ~250 km depth, although peak velocity reduction occurs at LVZ depths.

Posterior distributions of ξ are very consistent between cratons (Figure 1; Figures S16 and S17 in Supporting Information S1). We observe a positive $\delta\xi$ anomaly that extends from the Moho to ~125–150 km depth in all cratons. Peak amplitudes vary between 5% and 21%, at 85.1–99.1 km depth. Below, median models contain no radial anisotropy, with very little evidence for any negative radial anisotropy, specifically, within the posterior. Elsewhere, away from continental cores, slow V_{SV} anomalies are observed until >250 km depth with variable radial anisotropic structure (Figures S18 and S19 in Supporting Information S1). For example, below the East Pacific Rise and western United States, there is only very limited evidence within the full posterior for positive radial anisotropy in the upper mantle—radial anisotropy is not required by the median model in this depth range.

Results from LSQR inversions (Figures S20–S23 in Supporting Information S1) show substantial differences to Bayesian results. Fast cratonic velocities are captured as broad anomalies of up to ~6% extending to ~250 km depth, with no evidence for a mid-lithospheric LVZ (Figure 1; Figures S20 and S21 in Supporting Information S1). While $\delta\xi$ profiles are largely positive above ~125 km depth, they do not return to zero in the crust and frequently show negative radial anisotropy at 150–250 km depth, with amplitudes varying with parameterization. Below ~250 km depth, $\delta\xi$ returns to close to zero. Negative $\delta\xi$ anomalies at mid-lithospheric depths look similar to results of inversions of isotropic synthetic data (Figure S12 in Supporting Information S1). Consequently, we argue that the negative $\delta\xi$ previously imaged below continental cores in the 150–250 km depth range is likely an artifact of LSQR inversion parameterization, particularly where V_{SV} and ξ are inverted for independently (e.g., Priestley et al., 2020).

3.2. Comparison With Studies Using Long and Short Period Data

While global models show weak agreement with our results (Figure 1; Figures S1–S5 in Supporting Information S1), continental-to-regional scale studies show some evidence for a mid-lithospheric LVZ and radial anisotropic layering in cratons (Figure 1; Figures S16 and S17 in Supporting Information S1). For example, seismic reflection/refraction lines across multiple continents indicate the presence of a widespread LVZ at ~100 km depth (Thybo, 2006; Thybo & Perchuć, 1997). Perhaps due to shorter periods (<40 s), finer parameterization and/or weaker regularization, some regional surface wave studies show evidence for an LVZ at similar mid-lithospheric depths in Baltica (Bruneton et al., 2004), North America (C.-W. Chen et al., 2007; H. Yuan & Romanowicz, 2010) and when coupled with converted phases (Calò et al., 2016; Eilon et al., 2018). Meanwhile, in Australia, dominantly positive radial anisotropy appears in the upper lithosphere, with weaker anisotropy below (Kennett et al., 2017). Here, the rapid change of anisotropic strength corresponds well with discontinuity depths observed in converted phase studies (Yoshizawa & Kennett, 2015).

In Figure 2 we compare the median profiles for V_{SV} and ξ from the Bayesian inversion results with a global database of negative velocity gradient (NVG) observations from point locations in previous S-to-p receiver function studies (see Supporting Information S1; Abt et al., 2010; Birkey et al., 2021; Bodin et al., 2014; Courtier & Revenaugh, 2006; Dündar et al., 2011; Ford et al., 2010, 2016; Geissler et al., 2010; Heit et al., 2007; Heuer et al., 2007; Kawakatsu et al., 2009; Krueger et al., 2021; Kumar, Kind, et al., 2005; Kumar, Yuan, et al., 2005; Kumar, Kind, et al., 2007; Kumar, Yuan, et al., 2007; Kumar et al., 2006, 2012, 2013; Li et al., 2004, 2007; Miller & Eaton, 2010; Mohsen et al., 2006; Revenaugh & Sipkin, 1994; Rychert & Shearer, 2009; Rychert et al., 2005, 2007; Saul et al., 2000; Selway et al., 2015; Sodoudi, Kind, et al., 2006; Sodoudi, Yuan, et al., 2006; Sodoudi et al., 2009; Wirth & Long, 2014; Wölbern et al., 2012; X. Yuan et al., 2006; J. Zhao et al., 2010; W. Zhao et al., 2011; Zheng & Romanowicz, 2012). There is little difference in the depth distribution of NVGs between Phanerozoic (Mean: 95.6 km, S.t.d: 29.4 km), Shield (Mean: 94.8 km, S.t.d: 24.7 km) and Craton (Mean: 92.3 km, S.t.d: 26.7 km) localities globally (Figure 2b). Where data is available, we compare the mean depth of NVGs observed within each of the 12 cratons studied, with the top and base of both the LVZ in the V_{SV} profile and positive anomaly in the $\delta\xi$ profile, defined by maximum/minimum gradients bounding these anomalies (Figures 2c and 2d). In all localities, the mean NVG depth exists within the LVZ, because the top and base of the LVZ consistently lie above and below the mean NVG depth, respectively. Furthermore, in all but one location, the NVG lies within the positive $\delta\xi$ zone. For all cratons, the top of the $\delta\xi$ anomaly lies above the mean NVG depth, while the base lies below the mean NVG depth in all but one instance. Therefore, NVGs are likely unrelated to a ξ interface. We find no correlation between the mean NVG depth and the minimum lithospheric δV_{SV} (peak velocity reduction in the LVZ), suggesting a variable thickness/heterogeneous LVZ. Furthermore, no correlation is present between the mean NVG depth and the depth of maximum $\delta\xi$, that is relatively uniform globally (~14 km range).

The tops of observed LVZs in our inversions likely reflect mid-lithospheric discontinuities in cratons. S-to-p receiver function studies record evidence for negative velocity gradients, consistent with the top of LVZs (Krueger et al., 2021). The top of the LVZs (blue circles Figure 2e) lie closest to the line $x = y$ ($X^2 = 28.9$) and are the most correlated with mean NVG depths (correlation coefficient = 0.68), of any interface studied in Figure 2. This is explored further in Section 4.

4. Discussion

4.1. Implications for Craton Formation

Broadly consistent positive radial anisotropy anomalies extending from the Moho to ∼125–150 km depth in 12 cratons (Figure 1; Figures S16 and S17 in Supporting Information S1) help to discern between previous models of craton formation (Aulbach, 2012; Lee, 2006; Lee et al., 2011). A craton formation model of horizontal terrane accretion and arc thickening (Jordan, 1978; Pearson et al., 2021; Priestley et al., 2020) would likely result in vertically orientated fabrics and consequently, negative radial anisotropy at lithospheric depths (e.g., Priestley et al., 2020). However, evidence for negative radial anisotropy is absent (Figure 1; Figures S16 and S17 in Supporting Information S1) and tests show that previous results may have been complicated by artifacts (Figures S12, S20, and S21 in Supporting Information S1), meaning this mechanism for craton formation is unfavorable. Underthrusting of oceanic plates to build thick continents (e.g., Pearson & Wittig, 2008; Simon et al., 2007) is supported by some evidence for steeply dipping mid-lithospheric boundaries at craton margins (e.g., Hopper & Fischer, 2015; Miller & Eaton, 2010). However, negatively buoyant oceanic lithosphere may preferentially subduct rather than subcrete (Arndt et al., 2009), and such a mechanism is hard to reconcile with the strong positive radial anisotropy observed in cratons (Figure 1; Figures S16 and S17 in Supporting Information S1). Although difficulties remain in explaining the depth difference between cratonic peridotite protoliths and their final equilibrium temperature (Lee et al., 2011), our results of a globally consistent ξ anomaly are most easily reconciled with a plume/underplating model for craton formation (Arndt et al., 2009; Griffin et al., 2003). Because upwelling plume material will spread laterally below a solid plate and subsequently cool, a preferential horizontal alignment of mineral fabrics will be established, leading to a clear $V_{SH} > V_{SV}$ signature in the upper layer of cratons, as is observed (Figure 1; Figures S16 and S17 in Supporting Information S1).

Tests (Figures S24–S26 in Supporting Information S1) show that extrinsic anisotropy, characterized by 40% variations in δV_{SV} with periodic 5 km thick layering, is required to reproduce a positive radial anisotropy anomaly of >10%. We consider this to be unrealistic, so conclude the upper layer anisotropy cannot be solely due to layering, and is intrinsically anisotropic, that is, characterized by preferential alignment of crystals. Furthermore, such extrinsic anisotropy cannot reproduce a V_{SV} profile containing an upper lithospheric LVZ. We image a fast velocity lower layer within cratons that lacks radial anisotropy (Figure 1; Figures S16 and S17 in Supporting Information S1), meaning it is likely cold, but it formed via a process unrelated to plume underplating. This suggests the lower isotropic layer formed after underplating terminated during times of less vigorous convection, consistent with thermal accretion mechanisms (Darbyshire et al., 2013; H. Yuan & Romanowicz, 2010) and/or reformation following removal (Hu et al., 2018; Liu et al., 2021).

4.2. Implications for Formation of Mid-Lithospheric Discontinuities

Imaged variable amplitude shallow lithospheric LVZs (Figure 1; Figures S16 and S17 in Supporting Information S1) also shed new light on craton development. Negative velocity gradients (NVGs), highlighted as negative amplitude arrivals on S-to-p receiver functions (SRFs), are observed intermittently from 50 to >150 km depth (Figure 2, e.g., Hua et al., 2023; Karato et al., 2015; Krueger et al., 2021; Rader et al., 2015; Selway et al., 2015). In young, thin lithosphere, this discontinuity may represent the lithosphere-asthenosphere boundary, but in old, thick cratonic lithosphere (>250 km), these NVGs are termed mid-lithospheric discontinuities (MLDs; Karato et al., 2015; Rader et al., 2015; Selway et al., 2015).

Numerous causal mechanisms of the MLD have been suggested (e.g., Selway et al., 2015). Smooth, cold cratonic geotherms render temperature and present-day partial melt insufficient to produce sharp NVGs and corresponding LVZs/MLDs observed above 150 km depth by SRFs or our inversions (e.g., Kumar et al., 2012; Krueger et al., 2021; Thybo, 2006; Figure 1; Figures S16 and S17 in Supporting Information S1). Spatially variable LVZs (Figure 1; Figures S16 and S17 in Supporting Information S1) and NVGs in SRFs (Krueger et al., 2021;

Figure 2), that also become shallower rather than deeper between Phanerozoic, Shield and Craton localities (95.6, 94.8, 92.3 km depth respectively), mean there is limited support for a ubiquitous MLD of sufficient amplitude produced by elastically accommodated grain boundary sliding, given its thermal dependence (e.g., Karato et al., 2015; Selway et al., 2015). Furthermore, a lack of consensus on continental anisotropic structure (e.g., Figures S1–S5 in Supporting Information S1) has rendered vertical changes in both azimuthal and radial anisotropy as unfavorable causes of the MLD (e.g., Ford et al., 2016; Rychert & Shearer, 2009; Wirth & Long, 2014; Yoshizawa & Kennett, 2015; H. Yuan & Romanowicz, 2010). Our results show cratonic MLDs exist within positive ξ anomalies, rather than at the anomaly base (Figure 2f) meaning cratonic MLDs are not caused by a change in radial anisotropy. Instead we require a horizontal interface in V_{SV} to produce cratonic NVGs/MLDs (e.g., Ford et al., 2016).

Although composition partially controls V_{SV} (Schutt & Lesher, 2006), a change in depletion level with depth is not easily reconciled with mantle xenoliths (e.g., Griffin et al., 2004) or craton formation mechanisms (Lee, 2006). However, lithospheric metasomatism leading to the accumulation of lower velocity volatile-bearing/hydrous phases or frozen-in melt below MLD depths (e.g., Aulbach et al., 2017; Fu et al., 2022; Saha et al., 2021; Sodoudi et al., 2013; Wölbern et al., 2012) presents a fruitful explanation for MLD formation, despite debate concerning the amplitude of plausible V_{SV} velocity drops (Saha & Dasgupta, 2019; Saha et al., 2018, 2021) compared to observations (2%–6%, e.g., Krueger et al., 2021). Because the MLD exists within the positive ξ layer, metasomatism (e.g., Bruneton et al., 2004) occurred after cratons were formed meaning, in contrast to Rader et al. (2015), the MLD was not the lithosphere-asthenosphere boundary of young, thin cratons in Archean times. Variable amplitude LVZs (Figure 1; Figures S16 and S17 in Supporting Information S1) and intermittent MLD observations (e.g., Krueger et al., 2021) imply cratons have witnessed variable post-formation modification, meaning MLD observations likely coincide with modified cratons characterized by a shallow lithospheric LVZ.

4.3. A Unified Model for Craton Formation and Evolution

In Figure 3, we propose a synthetic craton model including a mid-lithospheric LVZ within a positive radially anisotropic upper lithospheric layer. We explore whether this model explains our results and previous observations by inverting synthetic data using our Bayesian algorithm and forward modeling SRFs (see Section 2). A lithospheric LVZ (~10% instantaneous V_{SV} drop, inline with previous works, Hopper & Fischer, 2015) is recovered as a smoothly varying velocity profile akin to observations (Figure 1). The NVG atop the LVZ produces a negative amplitude arrival at ~90 km depth in the SRF stack, similar to observations (Figure 2). The base of the positively radially anisotropic layer and colocated V_{SV} increase with depth is not seen in the SRF stack, due to interference from the earlier-arriving phase at the period band used. The forward modeled synthetic data is also representative of observed cratonic data (Figures 3d and 3e). Tests show we cannot distinguish between an isotropic or extrinsically anisotropic LVZ, but SRF forward modeling is robust (Figures S27–S30 in Supporting Information S1).

Figure 4 shows our three-step interpretation of craton development. An upper, ~125–150 km thick, depleted layer is formed in the Archean by underplating from lateral spreading of plume material, producing a radially anisotropic signature common to all cratons. A lower layer lacking radial anisotropy, perhaps rich in diamonds (Garber et al., 2018; Walsh et al., 2023), is formed at later time through cooling and steady thickening to ~250–300 km depth. Finally, the diverse, recent history of continental cores yields variable levels of post-formation modification through metasomatism, producing a variable amplitude LVZ within the upper layer. Although our results cannot constrain the metasomatic reagent (i.e., fluid/melt; Saha & Dasgupta, 2019; Saha et al., 2018), the accumulation of frozen-in melt sills (Saha et al., 2021) can cause extrinsic anisotropy (Hansen et al., 2021) within the LVZ (Figure S27 in Supporting Information S1). This interpretation is consistent with the anisotropic peak that exists at LVZ depths (Figure 1; Figures S16 and S17 in Supporting Information S1).

5. Conclusions

By jointly inverting Rayleigh and Love surface wave dispersion data using a flexible Bayesian approach, we reveal evidence for a consistent positive radially anisotropic upper layer and isotropic lower layer within

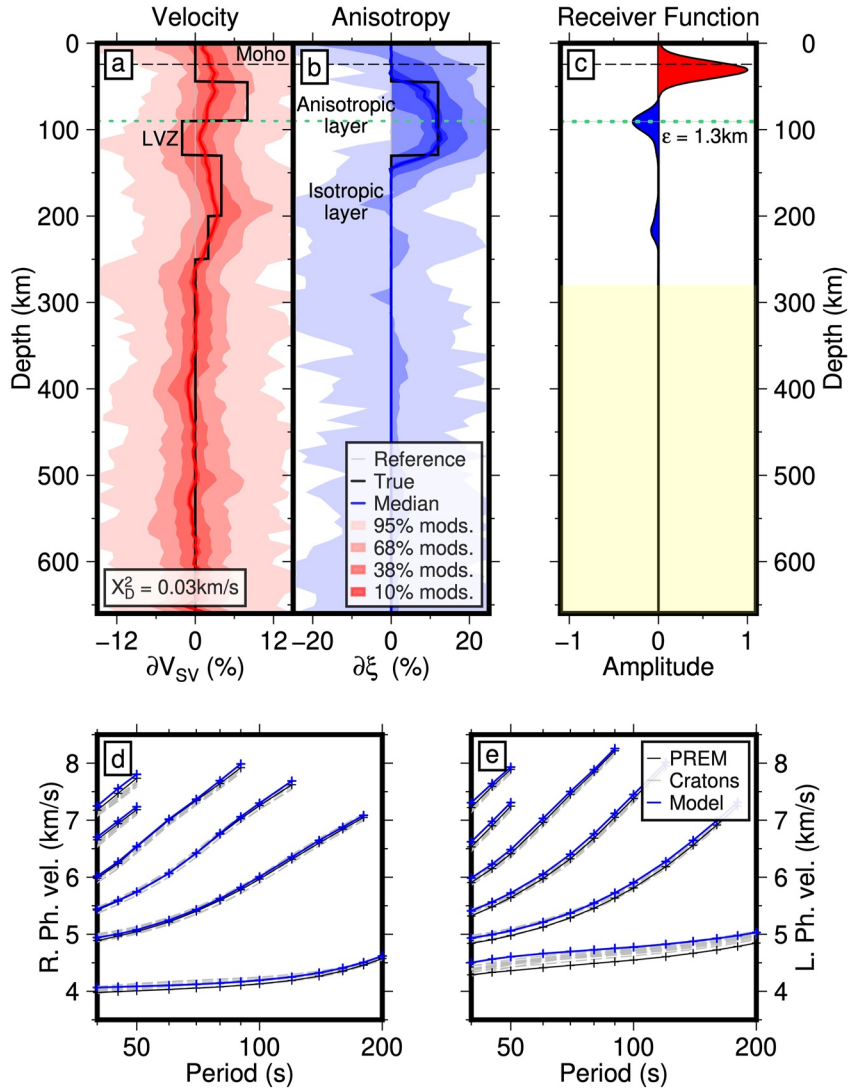

Figure 3. Posterior distributions for V_{SV} (a) and ξ (b) for proposed synthetic model (bold black line) with respect to isotropic reference model (gray line). The preferred median model for V_{SV} (red) and ξ (blue) is shown as a solid, bold line. Confidence intervals (percentage of models) are shown as varying shades of red (V_{SV}) and blue (ξ). Data misfit $\left(X_D^2\right)$ is also reported. S-to-p Receiver Function (SRF) stack (c) obtained from spectral element simulations (Axisem) using the proposed synthetic model (a, b). Green horizontal dashed lines show depth difference (ε) between input discontinuity and maximum amplitude on the SRF. Yellow shaded region is below SRF stacking depth. Rayleigh (d) and Love (e) fundamental and overtone (1–5) synthetic dispersion curves.

cratons. Our results also show evidence for a heterogeneous mid-lithospheric low velocity zone within the upper anisotropic layer, consistent with observations of negative velocity gradients from converted phase studies.

Consistent radial anisotropy results likely indicate a common two-stage formation mechanism for cratons. The positively anisotropic upper layer is best explained by Archean underplating. The lower isotropic layer may have formed later by steady thermal accretion. The variable amplitude low velocity zone in cratonic lithosphere and globally heterogeneous observations of mid-lithospheric discontinuities, that do not correspond to a change in radial anisotropy, suggest the MLD is best explained by metasomatism that occurred after craton formation terminated.

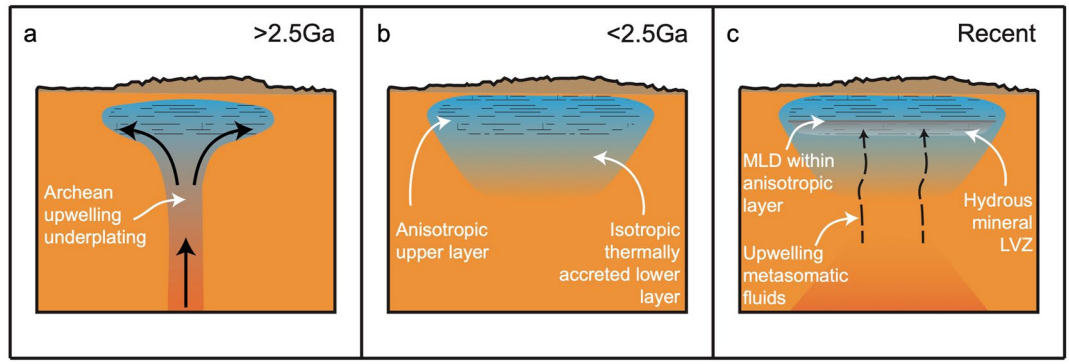

Figure 4. Schematic interpretation of craton development. (a) An upper, ~125 km thick, depleted layer is formed by Archean (>2.5 Ga) underplating from lateral spreading of plume material, producing radially anisotropic signature. (b) A lower isotropic layer is formed later (<2.5 Ga) through cooling and steady thickening to ~250–300 km depth. (c) Irregular post-formation cratonic history yields inconsistent metasomatic modification, producing a variable amplitude LVZ within the upper anisotropic layer.

Data Availability Statement

The data files, NVG database, software package and plotting codes are available (Boyce, 2023). Figures plotted using Generic Mapping Tools (https://www.generic-mapping-tools.org/).

Acknowledgments
T.B. is supported by the European Union Horizon 2020 research and innovation programme under Grant agreement 716542. S.D. and E.D. are supported by the French ANR project JIGSAW2 ANR-20-CE49-0001-01. The authors thank E. Rader, R. Kind, and H. Krueger for their help assembling the NVG database.

References

Abt, D. L., Fischer, K. M., French, S. W., Ford, H. A., Yuan, H., & Romanowicz, B. (2010). North American lithospheric discontinuity structure imaged by Ps and Sp receiver functions. *Journal of Geophysical Research*, *115*(B9), B09301. https://doi.org/10.1029/2009JB006914

Alder, C., Debayle, E., Bodin, T., Paul, A., Stehly, L., & Pedersen, H. (2021). Evidence for radial anisotropy in the lower crust of the Apennines from Bayesian ambient noise tomography in Europe. *Geophysical Journal International*, *226*(2), 941–967. https://doi.org/10.1093/gji/ggab066

Arndt, N. T., Coltice, N., Helmstaedt, H., & Gregoire, M. (2009). Origin of Archean subcontinental lithospheric mantle: Some petrological constraints. *Lithos*, *109*(1–2), 61–71. https://doi.org/10.1016/j.lithos.2008.10.019

Auer, L., Boschi, L., Becker, T. W., Nissen-Meyer, T., & Giardini, D. (2014). Savani: A variable resolution whole-mantle model of anisotropic shear velocity variations based on multiple data sets. *Journal of Geophysical Research: Solid Earth*, *119*(4), 3006–3034. https://doi.org/10.1002/2013jb010773

Aulbach, S. (2012). Craton nucleation and formation of thick lithospheric roots. *Lithos*, *149*, 16–30. https://doi.org/10.1016/j.lithos.2012.02.011

Aulbach, S., Massuyeau, M., & Gaillard, F. (2017). Origins of cratonic mantle discontinuities: A view from petrology, geochemistry and thermodynamic models. *Lithos*, *268*, 364–382. https://doi.org/10.1016/j.lithos.2016.11.004

Beghein, C., & Trampert, J. (2004). Probability density functions for radial anisotropy from fundamental mode surface wave data and the Neighbourhood Algorithm. *Geophysical Journal International*, *157*(3), 1163–1174. https://doi.org/10.1111/j.1365-246x.2004.02235.x

Birkey, A., Ford, H. A., Dabney, P., & Goldhagen, G. (2021). The lithospheric architecture of Australia from seismic receiver functions. *Journal of Geophysical Research: Solid Earth*, *126*(4), e2020JB020999. https://doi.org/10.1029/2020jb020999

Bodin, T., Leiva, J., Romanowicz, B., Maupin, V., & Yuan, H. (2016). Imaging anisotropic layering with Bayesian inversion of multiple data types. *Geophysical Journal International*, *206*(1), 605–629. https://doi.org/10.1093/gji/ggw124

Bodin, T., Sambridge, M., Rawlinson, N., & Arroucau, P. (2012). Transdimensional tomography with unknown data noise. *Geophysical Journal International*, *189*(3), 1536–1556. https://doi.org/10.1111/j.1365-246x.2012.05414.x

Bodin, T., Yuan, H., & Romanowicz, B. (2014). Inversion of receiver functions without deconvolution—Application to the Indian craton. *Geophysical Journal International*, *196*(2), 1025–1033. https://doi.org/10.1093/gji/ggt431

Boyce, A. (2023). Craton radial anisotropy and low velocity zones imaged with Bayesian and LSQR methods [Dataset]. Zenodo. https://doi.org/10.5281/zenodo.8167649

Bozdağ, E., & Trampert, J. (2008). On crustal corrections in surface wave tomography. *Geophysical Journal International*, *172*(3), 1066–1082. https://doi.org/10.1111/j.1365-246X.2007.03690.x

Bruneton, M., Pedersen, H. A., Vacher, P., Kukkonen, I. T., Arndt, N. T., Funke, S., et al. (2004). Layered lithospheric mantle in the central Baltic Shield from surface waves and xenolith analysis. *Earth and Planetary Science Letters*, *226*(1–2), 41–52. https://doi.org/10.1016/j.epsl.2004.07.034

Calò, M., Bodin, T., & Romanowicz, B. (2016). Layered structure in the upper mantle across North America from joint inversion of long and short period seismic data. *Earth and Planetary Science Letters*, *449*, 164–175. https://doi.org/10.1016/j.epsl.2016.05.054

Chang, S. J., Ferreira, A. M. G., Ritsema, J., Van Heijst, H.-J., & Woodhouse, J. H. (2014). Global radially anisotropic mantle structure from multiple datasets: A review, current challenges, and outlook. *Tectonophysics*, *617*, 1–19. https://doi.org/10.1016/j.tecto.2014.01.033

Chang, S. J., Ferreira, A. M. G., Ritsema, J., Van Heijst, H.-J., & Woodhouse, J. H. (2015). Joint inversion for global isotropic and radially anisotropic mantle structure including crustal thickness perturbations. *Journal of Geophysical Research: Solid Earth*, *120*(6), 4278–4300. https://doi.org/10.1002/2014jb011824

Chen, C.-W., Rondenay, S., Weeraratne, D. S., & Snyder, D. B. (2007). New constraints on the upper mantle structure of the Slave craton from Rayleigh wave inversion. *Geophysical Research Letters*, *34*(10), L10301. https://doi.org/10.1029/2007gl029535

Chen, L. (2017). Layering of subcontinental lithospheric mantle. *Science Bulletin*, *62*(14), 1030–1034. https://doi.org/10.1016/j.scib.2017.06.003

Courtier, A. M., & Revenaugh, J. (2006). Earth's deep water cycle. *Geophysical Monograph Series*, 181–193. https://doi.org/10.1029/168gm14

Darbyshire, F. A., Eaton, D. W., & Bastow, I. D. (2013). Seismic imaging of the lithosphere beneath Hudson Bay: Episodic growth of the Laurentian mantle keel. *Earth and Planetary Science Letters*, *373*, 179–193. https://doi.org/10.1016/j.epsl.2013.05.002

Debayle, E., & Kennett, B. (2000). Anisotropy in the Australasian upper mantle from Love and Rayleigh waveform inversion. *Earth and Planetary Science Letters*, *184*(1), 339–351. https://doi.org/10.1016/s0012-821x(00)00314-9

Debayle, E., & Ricard, Y. (2012). A global shear velocity model of the upper mantle from fundamental and higher Rayleigh mode measurements. *Journal of Geophysical Research*, *117*(B10), B10308. https://doi.org/10.1029/2012jb009288

Dündar, S., Kind, R., Yuan, X., Bulut, F., Sodoudi, F., Heit, B., et al. (2011). Receiver function images of the base of the lithosphere in the Alboran Sea region. *Geophysical Journal International*, *187*(2), 1019–1026. https://doi.org/10.1111/j.1365-246x.2011.05216.x

Durand, S., Debayle, E., & Ricard, Y. (2015). Rayleigh wave phase velocity and error maps up to the fifth overtone [Dataset]. Geophysical Research Letters, *42*(9), 3266–3272. https://doi.org/10.1002/2015gl063700

Dziewonski, A. M., & Anderson, D. L. (1981). Preliminary reference Earth model. *Physics of the Earth and Planetary Interiors*, *25*(4), 297–356. https://doi.org/10.1016/0031-9201(81)90046-7

Eilon, Z., Fischer, K. M., & Dalton, C. A. (2018). An adaptive Bayesian inversion for upper-mantle structure using surface waves and scattered body waves. *Geophysical Journal International*, *214*(1), 232–253. https://doi.org/10.1093/gji/ggy137

Ford, H. A., Fischer, K. M., Abt, D. L., Rychert, C. A., & Elkins-Tanton, L. T. (2010). The lithosphere–asthenosphere boundary and cratonic lithospheric layering beneath Australia from Sp wave imaging. *Earth and Planetary Science Letters*, *300*(3–4), 299–310. https://doi.org/10.1016/j.epsl.2010.10.007

Ford, H. A., Long, M. D., & Wirth, E. A. (2016). Midlithospheric discontinuities and complex anisotropic layering in the mantle lithosphere beneath the Wyoming and Superior Provinces. *Journal of Geophysical Research: Solid Earth*, *121*(9), 6675–6697. https://doi.org/10.1002/2016jb012978

French, S. W., & Romanowicz, B. (2014). Whole-mantle radially anisotropic shear velocity structure from spectral-element waveform tomography. *Geophysical Journal International*, *199*(3), 1303–1327. https://doi.org/10.1093/gji/ggu334

Fu, H., Li, Z., & Chen, L. (2022). Continental mid-lithosphere discontinuity: A water collector during craton evolution. *Geophysical Research Letters*, *49*(23), e2022GL101569. https://doi.org/10.1029/2022gl101569

Garber, J. M., Maurya, S., Hernandez, J., Duncan, M. S., Zeng, L., Zhang, H. L., et al. (2018). Multidisciplinary constraints on the abundance of diamond and eclogite in the cratonic lithosphere. *Geochemistry, Geophysics, Geosystems*, *19*(7), 2062–2086. https://doi.org/10.1029/2018gc007534

Geissler, W. H., Sodoudi, F., & Kind, R. (2010). Thickness of the central and eastern European lithosphere as seen by S receiver functions. *Geophysical Journal International*, *181*(2), 604–634. https://doi.org/10.1111/j.1365-246x.2010.04548.x

Griffin, W. L., Doyle, B. J., Ryan, C. G., Pearson, N. J., Suzanne, Y. O., Davies, R., et al. (1999). Layered mantle lithosphere in the Lac de Gras Area, Slave Craton: Composition, structure and origin. *Journal of Petrology*, *40*(5), 705–727. https://doi.org/10.1093/petroj/40.5.705

Griffin, W. L., O'Reilly, S. Y., Abe, N., Aulbach, S., Davies, R. M., Pearson, N. J., et al. (2003). The origin and evolution of Archean lithospheric mantle. *Precambrian Research*, *127*(1–3), 19–41. https://doi.org/10.1016/S0301-9268(03)00180-3

Griffin, W. L., O'Reilly, S. Y., Doyle, B. J., Pearson, N. J., Coopersmith, H., Kivi, K., et al. (2004). Lithosphere mapping beneath the North American plate. *Lithos*, *77*(1), 873–922. https://doi.org/10.1016/j.lithos.2004.03.034

Gung, Y., Panning, M. P., & Romanowicz, B. (2003). Global anisotropy and the thickness of continents. *Nature*, *422*(6933), 707–711. https://doi.org/10.1038/nature01559

Hansen, L. N., Faccenda, M., & Warren, J. M. (2021). A review of mechanisms generating seismic anisotropy in the upper mantle. *Physics of the Earth and Planetary Interiors*, *313*, 106662. https://doi.org/10.1016/j.pepi.2021.106662

Hasterok, D., Halpin, J. A., Collins, A. S., Hand, M., Kreemer, C., Gard, M. G., & Glorie, S. (2022). New maps of global geological provinces and tectonic plates. *Earth-Science Reviews*, *231*, 104069. https://doi.org/10.1016/j.earscirev.2022.104069

Heit, B., Sodoudi, F., Yuan, X., Bianchi, M., & Kind, R. (2007). An S receiver function analysis of the lithospheric structure in South America. *Geophysical Research Letters*, *34*(14), L14307. https://doi.org/10.1029/2007gl030317

Heuer, B., Kämpf, H., Kind, R., & Geissler, W. H. (2007). Seismic evidence for whole lithosphere separation between Saxothuringian and Moldanubian tectonic units in central Europe. *Geophysical Research Letters*, *34*(9), L09304. https://doi.org/10.1029/2006gl029188

Ho, T., Priestley, K., & Debayle, E. (2016). A global horizontal shear velocity model of the upper mantle from multimode Love wave measurements [Dataset]. Geophysical Journal International, *207*(1), 542–561. https://doi.org/10.1093/gji/ggw292

Hoffman, P. F. (1990). Geological constraints on the origin of the mantle root beneath the Canadian shield. *Philosophical Transactions of the Royal Society of London—A*, *331*(1620), 523–532. https://doi.org/10.1098/rsta.1990.0087

Hopper, E., & Fischer, K. M. (2015). The meaning of midlithospheric discontinuities: A case study in the northern U.S. craton. *Geochemistry, Geophysics, Geosystems*, *16*(12), 4057–4083. https://doi.org/10.1002/2015gc006030

Hu, J., Liu, L., Faccenda, M., Zhou, Q., Fischer, K. M., Marshak, S., & Lundstrom, C. (2018). Modification of the Western Gondwana craton by plume–lithosphere interaction. *Nature Geoscience*, *11*(3), 203–210. https://doi.org/10.1038/s41561-018-0064-1

Hua, J., Fischer, K. M., Becker, T. W., Gazel, E., & Hirth, G. (2023). Asthenospheric low-velocity zone consistent with globally prevalent partial melting. *Nature Geoscience*, *16*(2), 175–181. https://doi.org/10.1038/s41561-022-01116-9

Jordan, T. H. (1978). Composition and development of the continental tectosphere. *Nature*, *274*(5671), 544–548. https://doi.org/10.1038/274544a0

Karato, S., Olugboji, T., & Park, J. (2015). Mechanisms and geologic significance of the mid-lithosphere discontinuity in the continents. *Nature Geoscience*, *8*(7), 509–514. https://doi.org/10.1038/ngeo2462

Kawakatsu, H., Kumar, P., Takei, Y., Shinohara, M., Kanazawa, T., Araki, E., & Suyehiro, K. (2009). Seismic evidence for sharp lithosphere-asthenosphere boundaries of oceanic plates. *Science*, *324*(5926), 499–502. https://doi.org/10.1126/science.1169499

Kennett, B. L. N., Yoshizawa, K., & Furumura, T. (2017). Interactions of multi-scale heterogeneity in the lithosphere: Australia. *Tectonophysics*, *717*, 193–213. https://doi.org/10.1016/j.tecto.2017.07.009

Krueger, H. E., Gama, I., & Fischer, K. M. (2021). Global patterns in cratonic mid-lithospheric discontinuities from Sp receiver functions. *Geochemistry, Geophysics, Geosystems*, *22*(6), e2021GC009819. https://doi.org/10.1029/2021gc009819

Kumar, P., Kind, R., Hanka, W., Wylegalla, K., Reigber, C., Yuan, X., et al. (2005). The lithosphere–asthenosphere boundary in the North-West Atlantic region. *Earth and Planetary Science Letters*, *236*(1–2), 249–257. https://doi.org/10.1016/j.epsl.2005.05.029

Kumar, P., Kind, R., Priestley, K., & Dahl-Jensen, T. (2007). Crustal structure of Iceland and Greenland from receiver function studies. *Journal of Geophysical Research*, *112*(B3), B03301. https://doi.org/10.1029/2005jb003991

Kumar, P., Kumar, M. R., Srijayanthi, G., Arora, K., Srinagesh, D., Chadha, R. K., & Sen, M. K. (2013). Imaging the lithosphere-asthenosphere boundary of the Indian plate using converted wave techniques. *Journal of Geophysical Research: Solid Earth*, *118*(10), 5307–5319. https://doi.org/10.1002/jgrb.50366

Kumar, P., Yuan, X., Kind, R., & Kosarev, G. (2005). The lithosphere-asthenosphere boundary in the Tien Shan-Karakoram region from S receiver functions: Evidence for continental subduction. *Geophysical Research Letters*, *32*(7), L07305. https://doi.org/10.1029/2004gl022291

Kumar, P., Yuan, X., Kind, R., & Mechie, J. (2012). The lithosphere-asthenosphere boundary observed with USArray receiver functions. *Solid Earth*, *3*(1), 149–159. https://doi.org/10.5194/se-3-149-2012

Kumar, P., Yuan, X., Kind, R., & Ni, J. (2006). Imaging the colliding Indian and Asian lithospheric plates beneath Tibet. *Journal of Geophysical Research*, *111*(B6), B06308. https://doi.org/10.1029/2005jb003930

Kumar, P., Yuan, X., Kumar, M. R., Kind, R., Li, X., & Chadha, R. K. (2007). The rapid drift of the Indian tectonic plate. *Nature*, *449*(7164), 894–897. https://doi.org/10.1038/nature06214

Kustowski, B., Ekström, G., & Dziewoński, A. M. (2008). Anisotropic shear-wave velocity structure of the Earth's mantle: A global model. *Journal of Geophysical Research*, *113*(B6), B06306. https://doi.org/10.1029/2007jb005169

Laske, G., Masters, G., Ma, Z., & Pasyanos, M. E. (2013). Update on CRUST1.0—A 1-degree global model of Earth's crust. In *Geophysical research abstracts* (Vol. 15, p. EGU2013-2658). abstract egu2013-2658.

Lee, C.-T. A. (2006). Geochemical/petrologic constraints on the origin of cratonic mantle. In K. Benn, J.-C. Mareschal, & K. C. Condie (Eds.), *Archean geodynamics and environments* (pp. 89–114). American Geophysical Union (AGU). https://doi.org/10.1029/164GM08

Lee, C.-T. A., Luffi, P., & Chin, E. J. (2011). Building and destroying continental mantle. *Annual Review of Earth and Planetary Sciences*, *39*(1), 59–90. https://doi.org/10.1146/annurev-earth-040610-133505

Lekić, V., & Romanowicz, B. (2011). Inferring upper-mantle structure by full waveform tomography with the spectral element method. *Geophysical Journal International*, *185*(2), 799–831. https://doi.org/10.1111/j.1365-246X.2011.04969.x

Levin, V., Lebedev, S., Fullea, J., Li, Y., & Chen, X. (2023). Defining continental lithosphere as a layer with abundant frozen-in structures that scatter seismic waves. *Journal of Geophysical Research: Solid Earth*, *128*(7), e2022JB026309. https://doi.org/10.1029/2022jb026309

Li, X., Kind, R., Yuan, X., Wölbern, I., & Hanka, W. (2004). Rejuvenation of the lithosphere by the Hawaiian plume. *Nature*, *427*(6977), 827–829. https://doi.org/10.1038/nature02349

Li, X., Yuan, X., & Kind, R. (2007). The lithosphere–asthenosphere boundary beneath the western United States. *Geophysical Journal International*, *170*(2), 700–710. https://doi.org/10.1111/j.1365-246x.2007.03428.x

Ligorría, J., & Ammon, C. (1999). Iterative deconvolution and receiver-function estimation. *Bulletin of the Seismological Society of America*, *89*(5), 1395–1400. https://doi.org/10.1785/bssa0890051395

Liu, J., Pearson, D. G., Wang, L. H., Mather, K. A., Kjarsgaard, B. A., Schaeffer, A. J., et al. (2021). Plume-driven recratonization of deep continental lithospheric mantle. *Nature*, *592*(7856), 732–736. https://doi.org/10.1038/s41586-021-03395-5

Masters, G., Woodhouse, J. H., & Freeman, G. (2011). Mineos v1.0.2 [Software]. Computational Infrastructure for Geodynamics. (Published under the GPL2 license) Retrieved from https://geodynamics.org/cig/software/mineos/

Megnin, C., & Romanowicz, B. (2000). The three-dimensional shear velocity structure of the mantle from the inversion of body, surface and higher-mode waveforms. *Geophysical Journal International*, *143*(3), 709–728. https://doi.org/10.1046/j.1365-246X.2000.00298.x

Miller, M. S., & Eaton, D. W. (2010). Formation of cratonic mantle keels by arc accretion: Evidence from S receiver functions. *Geophysical Research Letters*, *37*(18), L18305. https://doi.org/10.1029/2010GL044366

Mohsen, A., Kind, R., Sobolev, S. V., & Weber, M., & the DESERT Group. (2006). Thickness of the lithosphere east of the Dead Sea Transform. *Geophysical Journal International*, *167*(2), 845–852. https://doi.org/10.1111/j.1365-246x.2006.03185.x

Moulik, P., & Ekström, G. (2014). An anisotropic shear velocity model of the Earth's mantle using normal modes, body waves, surface waves and long-period waveforms. *Geophysical Journal International*, *199*(3), 1713–1738. https://doi.org/10.1093/gji/ggu356

Nissen-Meyer, T., van Driel, M., Stähler, S. C., Hosseini, K., Hempel, S., Auer, L., et al. (2014). AxiSEM: Broadband 3-D seismic wavefields in axisymmetric media. *Solid Earth*, *5*(1), 425–445. https://doi.org/10.5194/se-5-425-2014

Panning, M. P., Lekić, V., & Romanowicz, B. (2010). Importance of crustal corrections in the development of a new global model of radial anisotropy. *Journal of Geophysical Research*, *115*(B12), B12325. https://doi.org/10.1029/2010jb007520

Pearson, D. G., Scott, J. M., Liu, J., Schaeffer, A., Wang, L. H., van Hunen, J., et al. (2021). Deep continental roots and cratons. *Nature*, *596*(7871), 199–210. https://doi.org/10.1038/s41586-021-03600-5

Pearson, D. G., & Wittig, N. (2008). Formation of Archaean continental lithosphere and its diamonds: The root of the problem. *Journal of the Geological Society London*, *165*(5), 895–914. https://doi.org/10.1144/0016-76492008-003

Priestley, K., Ho, T., & McKenzie, D. (2020). The formation of continental roots. *Geology*, *49*(2), 190–194. https://doi.org/10.1130/G47696.1

Priestley, K., McKenzie, D., & Ho, T. (2019). A lithosphere–asthenosphere boundary—A global model derived from multimode surface-wave tomography and petrology. In H. Yuan, & B. Romanowicz (Eds.), *Lithospheric discontinuities*, *Geophysical monograph* (1st ed., Vols, Vol. 239, pp. 111–123). American Geophysical Union and John Wiley & Sons, Inc. https://doi.org/10.1002/9781119249740.ch6

Rader, E., Emry, E., Schmerr, N., Frost, D., Cheng, C., Menard, J., et al. (2015). Characterization and petrological constraints of the midlithospheric discontinuity. *Geochemistry, Geophysics, Geosystems*, *16*(10), 3484–3504. https://doi.org/10.1002/2015gc005943

Revenaugh, J., & Sipkin, S. A. (1994). Mantle discontinuity structure beneath China. *Journal of Geophysical Research*, *99*(B11), 21911–21927. https://doi.org/10.1029/94jb01850

Rychert, C. A., Fischer, K. M., & Rondenay, S. (2005). A sharp lithosphere–asthenosphere boundary imaged beneath eastern North America. *Nature*, *436*(7050), 542–545. https://doi.org/10.1038/nature03904

Rychert, C. A., Rondenay, S., & Fischer, K. M. (2007). P-to-S and S-to-P imaging of a sharp lithosphere-asthenosphere boundary beneath eastern North America. *Journal of Geophysical Research*, *112*(B8), B08314. https://doi.org/10.1029/2006jb004619

Rychert, C. A., & Shearer, P. M. (2009). A global view of the lithosphere-asthenosphere boundary. *Science*, *324*(5926), 495–498. https://doi.org/10.1126/science.1169754

Saha, S., & Dasgupta, R. (2019). Phase relations of a depleted peridotite fluxed by a CO_2-H_2O fluid—Implications for the stability of partial melts versus volatile-bearing mineral phases in the cratonic mantle. *Journal of Geophysical Research: Solid Earth*, *124*(10), 10089–10106. https://doi.org/10.1029/2019jb017653

Saha, S., Dasgupta, R., & Tsuno, K. (2018). High pressure phase relations of a depleted peridotite fluxed by CO_2-H_2O-bearing siliceous melts and the origin of mid-lithospheric discontinuity. *Geochemistry, Geophysics, Geosystems*, *19*(3), 595–620. https://doi.org/10.1002/2017gc007233

Saha, S., Peng, Y., Dasgupta, R., Mookherjee, M., & Fischer, K. M. (2021). Assessing the presence of volatile-bearing mineral phases in the cratonic mantle as a possible cause of mid-lithospheric discontinuities. *Earth and Planetary Science Letters*, *553*, 116602. https://doi.org/10.1016/j.epsl.2020.116602

Saul, J., Kumar, M. R., & Sarkar, D. (2000). Lithospheric and upper mantle structure of the Indian Shield, from teleseismic receiver functions. *Geophysical Research Letters*, *27*(16), 2357–2360. https://doi.org/10.1029/1999gl011128

Schutt, D. L., & Lesher, C. E. (2006). Effects of melt depletion on the density and seismic velocity of garnet and spinel lherzolite. *Journal of Geophysical Research*, *111*(B5), B05401. https://doi.org/10.1029/2003JB002950

Selway, K., Ford, H., & Kelemen, P. (2015). The seismic mid-lithosphere discontinuity. *Earth and Planetary Science Letters*, *414*, 45–57. https://doi.org/10.1016/j.epsl.2014.12.029

Simon, N. S. C., Carlson, R. W., Pearson, D. G., & Davies, G. R. (2007). The origin and evolution of the Kaapvaal cratonic lithospheric mantle. *Journal of Petrology*, *48*(3), 589–625. https://doi.org/10.1093/petrology/egl074

Sodoudi, F., Kind, R., Hatzfeld, D., Priestley, K., Hanka, W., Wylegalla, K., et al. (2006). Lithospheric structure of the Aegean obtained from P and S receiver functions. *Journal of Geophysical Research*, *111*(B12), B12307. https://doi.org/10.1029/2005jb003932

Sodoudi, F., Yuan, X., Kind, R., Heit, B., & Sadidkhouy, A. (2009). Evidence for a missing crustal root and a thin lithosphere beneath the Central Alborz by receiver function studies. *Geophysical Journal International*, *177*(2), 733–742. https://doi.org/10.1111/j.1365-246x.2009.04115.x

Sodoudi, F., Yuan, X., Kind, R., Lebedev, S., Adam, J. M., Kästle, E., & Tilmann, F. (2013). Seismic evidence for stratification in composition and anisotropic fabric within the thick lithosphere of Kalahari Craton. *Geochemistry, Geophysics, Geosystems*, *14*(12), 5393–5412. https://doi.org/10.1002/2013gc004955

Sodoudi, F., Yuan, X., Liu, Q., Kind, R., & Chen, J. (2006). Lithospheric thickness beneath the Dabie Shan, central eastern China from S receiver functions. *Geophysical Journal International*, *166*(3), 1363–1367. https://doi.org/10.1111/j.1365-246x.2006.03080.x

Tarantola, A., & Valette, B. (1982). Generalized nonlinear inverse problems solved using the least squares criterion. *Reviews of Geophysics*, *20*(2), 219–232. https://doi.org/10.1029/rg020i002p00219

Tesoniero, A., Auer, L., Boschi, L., & Cammarano, F. (2015). Hydration of marginal basins and compositional variations within the continental lithospheric mantle inferred from a new global model of shear and compressional velocity. *Journal of Geophysical Research: Solid Earth*, *120*(11), 7789–7813. https://doi.org/10.1002/2015jb012026

Thybo, H. (2006). The heterogeneous upper mantle low velocity zone. *Tectonophysics*, *416*(1–4), 53–79. https://doi.org/10.1016/j.tecto.2005.11.021

Thybo, H., & Perchuć, E. (1997). The seismic 8° discontinuity and partial melting in continental mantle. *Science*, *275*(5306), 1626–1629. https://doi.org/10.1126/science.275.5306.1626

Walsh, C., Kamber, B. S., & Tomlinson, E. L. (2023). Deep, ultra-hot-melting residues as cradles of mantle diamond. *Nature*, *615*(7952), 450–454. https://doi.org/10.1038/s41586-022-05665-2

Wirth, E. A., & Long, M. D. (2014). A contrast in anisotropy across mid-lithospheric discontinuities beneath the central United States—A relic of craton formation. *Geology*, *42*(10), 851–854. https://doi.org/10.1130/g35804.1

Wittlinger, G., & Farra, V. (2007). Converted waves reveal a thick and layered tectosphere beneath the Kalahari super-craton. *Earth and Planetary Science Letters*, *254*(3–4), 404–415. https://doi.org/10.1016/j.epsl.2006.11.048

Wölbern, I., Rümpker, G., Link, K., & Sodoudi, F. (2012). Melt infiltration of the lower lithosphere beneath the Tanzania craton and the Albertine rift inferred from S receiver functions. *Geochemistry, Geophysics, Geosystems*, *13*(8), Q0AK08. https://doi.org/10.1029/2012gc004167

Yoshizawa, K., & Kennett, B. L. N. (2015). The lithosphere-asthenosphere transition and radial anisotropy beneath the Australian continent. *Geophysical Research Letters*, *42*(10), 3839–3846. https://doi.org/10.1002/2015gl063845

Yuan, H., & Bodin, T. (2018). A probabilistic shear wave velocity model of the crust in the central West Australian craton constrained by transdimensional inversion of ambient noise dispersion. *Tectonics*, *37*(7), 1994–2012. https://doi.org/10.1029/2017tc004834

Yuan, H., & Romanowicz, B. (2010). Lithospheric layering in the North American craton. *Nature*, *466*(7310), 1063–1068. https://doi.org/10.1111/j.1365-246X.2010.04901.x

Yuan, X., Kind, R., Li, X., & Wang, R. (2006). The S receiver functions: Synthetics and data example. *Geophysical Journal International*, *165*(2), 555–564. https://doi.org/10.1111/j.1365-246X.2006.02885.x

Zhao, J., Yuan, X., Liu, H., Kumar, P., Pei, S., Kind, R., et al. (2010). The boundary between the Indian and Asian tectonic plates below Tibet. *Proceedings of the National Academy of Sciences of the United States of America*, *107*(25), 11229–11233. https://doi.org/10.1073/pnas.1001921107

Zhao, W., Kumar, P., Mechie, J., Kind, R., Meissner, R., Wu, Z., et al. (2011). Tibetan plate overriding the Asian plate in central and northern Tibet. *Nature Geoscience*, *4*(12), 870–873. https://doi.org/10.1038/ngeo1309

Zheng, Z., & Romanowicz, B. (2012). Do double 'SS precursors' mean double discontinuities? *Geophysical Journal International*, *191*(3), 1361–1373. https://doi.org/10.1111/j.1365-246x.2012.05683.x